

# Rapid parameter estimation of discrete decaying signals using autoencoder networks

Jim C. Visschers,<sup>1, 2, \*</sup> Dmitry Budker,<sup>1, 2, 3</sup> and Lykourgos Bougas<sup>1, 2, †</sup>

<sup>1</sup>*Institut für Physik, Johannes Gutenberg Universität-Mainz, 55128 Mainz, Germany*

<sup>2</sup>*Helmholtz-Institut Mainz, GSI Helmholtzzentrum für Schwerionenforschung GmbH, Mainz 55128, Germany*

<sup>3</sup>*Department of Physics, University of California, Berkeley, California 94720-300, USA*

(Dated: December 24, 2024)

In this work we demonstrate the use of autoencoder networks for rapid extraction of the signal parameters of discretely sampled signals. In particular, we use dense autoencoder networks to extract the parameters of interest from exponentially decaying signals and decaying oscillations. Using a three-stage training method and careful choice of the neural network size, we are able to retrieve the relevant signal parameters directly from the latent space of the autoencoder network at significantly improved rates compared to traditional algorithmic signal-analysis approaches. We show that the achievable precision and accuracy of this method of analysis is similar to conventional, algorithm-based signal analysis methods, by demonstrating that, the extracted signal parameters are approaching their fundamental parameter estimation limit as provided by the Cramér-Rao lower bound. Furthermore, we demonstrate that autoencoder networks are able to achieve signal analysis, and, hence, parameter extraction, at rates of 75 kHz, orders -of- magnitude faster than conventional techniques with equal precision. Finally, we explore the limitations of our approach, demonstrating that analysis rates of >200 kHz are feasible with further optimization of the transfer rate between the data-acquisition system and data-analysis system.

## Contents

I. Introduction	1
II. Theory	2
A. Dense autoencoder neural networks	2
B. Model signals	4
1. Exponentially decaying signals	4
2. Decaying oscillations	4
3. Signal-to-noise ratio	4
4. Cramér-Rao lower bound	4
III. Methods	4
A. Simulated signals and data-sets	4
B. Dense autoencoder networks	5
C. Signal reconstruction and parameter extraction	5
D. Training protocol	5
IV. Results	6
A. Exponentially decaying signals	6
B. Decaying oscillations	6
C. Complexity vs. calculation time	9
V. Outlook and conclusion	9
References	10

## I. Introduction

Machine learning (ML) is becoming a widespread method for the generation, and analysis of big data. ML uses networks of interconnected neurons (neural networks) that, much like real brains, recognize patterns in data structures [1, 2]. Generally, these neural networks are first trained in situations where the desired action/output of the network is known and subsequently used in similar, real world situations. Research fields where a precise mathematical description of the problem is difficult -if not impossible- stand much to gain from implementing ML solutions. Areas such as image processing [3, 4] or text generation and analysis [5] have seen innovations that would not have been possible without the implementation of ML.

In physical sciences, ML-based techniques are becoming more and more widespread (see Ref. [6] for an excellent review). Besides unlocking completely new innovations, ML techniques have been utilized in situations where finding solutions to physical problems requires a lot of computing effort using conventional methods. For example in fluid simulations, that would normally require solving the Navier–Stokes equations, ML can be used to predict the evolution of a fluid simulation [7], reducing the amount of computation time of these complex simulations significantly. Furthermore, neural networks have been used to simulate light scattering by multilayer nanoparticles and subsequent and subsequent design of these nanoparticles using backpropagation [8]. In spectroscopy, machine learning is used to classify spectroscopic data [9–11]. Another field where ML techniques find their way is in experiments with extremely high inference rates and low latency constraints, such as in high-performance detector triggers [12] (e.g. the ATLAS experiment at the LHC at CERN). In these experiments, field-programmable gate array implementations of ML

\* [jvisschers@uni-mainz.de](mailto:jvisschers@uni-mainz.de)

† [lybougas@uni-mainz.de](mailto:lybougas@uni-mainz.de)

techniques are used to create complex hardware triggers for events with sub-microsecond lifetimes.

However, ML techniques are notoriously opaque, meaning that, although they deliver desired results, our understanding of how the results are obtained and how patterns in data are detected by the underlying neural network is very limited, similar to the understanding of real brains. Often, little or no information on the physical system that is solved/simulated can be gained by studying the neural network itself, which is a significant drawback of these techniques. Furthermore, basic questions regarding the minimal amount of training data, or the optimal size of the underlying neural network required to obtain good precision for a pre-defined problem remain unanswered.

Signal-parameter estimation is an integral part of both fundamental and applied research. Precision, accuracy and speed are crucial for the real-time observation and control of fast, physical and chemical processes. In the development of portable instruments, real-time data streaming with minimal computational costs is essential. A multitude of research fields rely on determination of time constants and frequencies of decaying signals, such examples include: nuclear magnetic resonance (NMR) [13] where molecular structures are analysed from precise determination of the frequency and decay constant of a damped sinusoidal signal generated by nuclear spins in magnetic fields; free-induction-decay (FID) optical magnetometry [14–19] where magnetic sensitivities depend on the precision of the measurement of the oscillating frequency; and cavity-enhanced spectroscopy and sensing methods [20–24] which rely on the detection of variations in the decay constant of optical cavities to identify trace gasses, measure absorption cross sections or observe chemical reactions in real time. Other cavity-enhanced methods, such as cavity ring-down polarimetry (CRDP) [25–32] and -ellipsometry (CRDE) [33–36], measure birefringence and/or dichorism of an optical medium through the precise estimation of signal-decay time and the beat frequency of polarization signals.

All the aforementioned methods require significant data processing to determine their relevant signal parameters. Optimizing sensitivity and minimizing computational costs is usually done by averaging multiple, consecutive measurements, sacrificing time-dynamic resolution. Therefore, it is imperative that one considers the sampling and acquisition rates of an instrument and balances that against the computational costs (calculation time) to analyze the acquired data, the time scales of relevant dynamics to be observed and the requirement to see those dynamics in real time. In cavity-enhanced spectroscopy, and CRDP/CRDE techniques in particular, the decay times of interest are typically in the  $10^{-7} - 10^{-5}$  s range, a few orders of magnitude smaller than the typical decay times of NMR experiments ( $10^{-2} - 10^1$  s) or FID optical magnetometry techniques ( $10^{-3} - 10^1$  s). As such, analysis methods that are sufficiently fast for the real-time analysis of single measurements of NMR or

FID magnetometry experiments do not have the capability to offer real-time analysis in situations where the relevant time scales are much smaller than ms, such is the case in many cavity-enhanced sensing methods, and CDRP/CDRE in particular.

Different time- and frequency-based computational methods for rapid parameter estimation have been demonstrated, and evaluated, for cavity ring-down (CRD) spectroscopy methods [37–39]. Among those, Fourier-transform methods on a field programmable gate arrays (FPGA) have demonstrated data-time analysis rates as high as 4.4 kHz [40]. Several works discuss time- and frequency-domain analysis algorithms for damped sinusoidal signals [41, 42] and we recently published a comparative study of three specific analysis methods of discretely sampled damped sinusoidal signals in terms of their speed, and attainable accuracy and precision [43].

In this work we demonstrate a ML based approach to extract the relevant signal parameters from experimentally relevant signals with well-defined functional form. More specifically, we use dense autoencoder networks to encode, extract parameters from, and subsequently reconstruct two types of discretely sampled, decaying signals: (1) exponentially decaying signals and (2) decaying oscillations. We evaluate the autoencoder network on its precision and accuracy in parameter extraction and compare its performance to the fundamental estimation limits of such signals given by the Cramér-Rao lower bound (CRLB). We show that the dense autoencoder network is able to reach analysis rates of 75 kHz of 1000 sample signals with cost-effective computational facilities making the ML method ideal for portable cavity-enhanced sensing instruments.

## II. Theory

### A. Dense autoencoder neural networks

A neural network is an ordered group of neurons that, much like the neurons in brains, communicate by signaling to each other. Each neuron has a number of incoming and outgoing connections from and to other neurons. Each connection has a strength (weight) and can be stimulating or inhibiting the response of the receiving neuron. To calculate the activity (value) of a neuron, one compares the sum of its weighted inputs to a neuron specific reference (bias). The difference is passed through an activation function which produces the output of the neuron [1, 2]. Initially, the weights and biases within a neural network start off randomly. As the neural network is trained, these weights and biases are altered to optimize the performance of the network with respect to the task it is asked to perform. The manner in which neurons are ordered and connected influence the capabilities of the network and a variety of network configurations with different purposes have been demonstrated [44].

A dense neural network is a network where the neurons are arranged in sequential layers and all the layers are fully connected. This means that every single neuron in one layer is connected to all neurons in the next

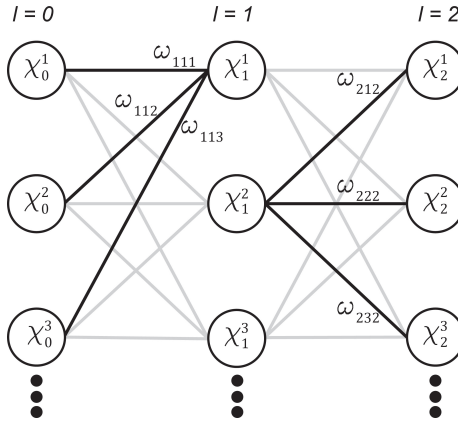


FIG. 1. Example of a dense neural network with  $L = 2$  layers. The first layer,  $l = 0$  is the input layer,  $l = 1$  a hidden layer and  $l = 2$  is the output layer.  $\chi_y^x$  specifies neuron  $x$  in layer  $y$ . Each neuron contains a bias and layer specific activation function (not illustrated).  $\omega_{y,x,z}$  denotes the weight (strength) between neuron  $x$  in layer  $y$  and neuron  $z$  in layer  $x - 1$ . For illustrative purposes, some connections have been highlighted and are shown with their appropriate weight. The output of the neuron depends on its inputs, weights and bias put through the activation function (Eq. 1).

layer. There are no neural connections within a layer or connections spanning multiple layers. An example of a dense neural network is shown in Fig. 1. For such a neural network, one can calculate its output as:

$$\text{for } l : 0 \rightarrow L$$

$$\vec{\chi}_{i+1} = \mathcal{F}_l \left( \omega_{l+1} \cdot \vec{\chi}_l - \vec{b}_l \right), \quad (1)$$

where  $L$  is the number of layers in the neural network (excluding the input layer),  $\vec{\chi}_l$  is the output of the network at layer  $l$ ,  $\omega_l$  is the weights matrix, and  $\vec{b}_l$  is the bias vector for the corresponding neurons of layer  $l$ . Finally,  $\mathcal{F}_l$  is the activation function of the network layer that acts piece-wise on each neuron in layer  $l$ . The input layer ( $l = 0$ ) has no bias or activation function. Autoencoders are symmetric, hourglass-shaped neural networks [45–49] (Fig. 2). This means that the number of neurons in the middle layer of the network is small compared to the number of neurons in the input and output layer of the neural network. The goal of the autoencoder network is to recreate its input signal. In the first half of the autoencoder network, it learns, to encode the input data into a lower dimensional representation. In the second half, the autoencoder network learns, to subsequently decode that lower dimensional representation and reconstruct the original signal with minimal losses. The middle layer of the network, in which the maximal compression of the signal takes place, is called the latent space. The latent representation of the original signal can be extracted from the latent space. Autoencoder networks are typically used in data compression [48] and de-noising [49].

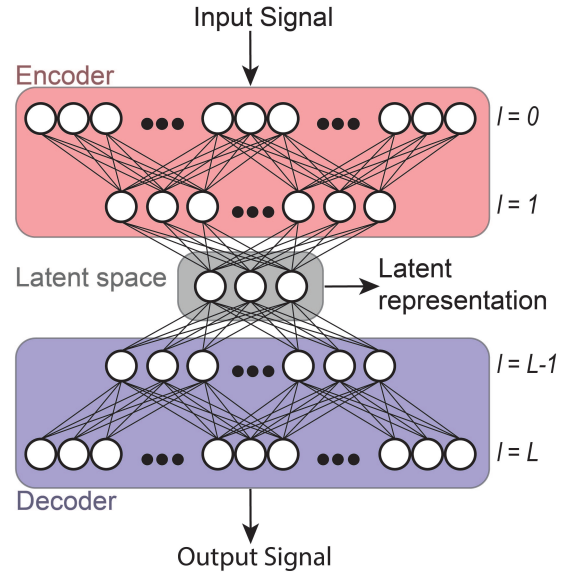


FIG. 2. Example of an autoencoder neural network with  $L$  layers. Signals are fed to the encoder, which compresses the data into a limited number of parameters after which the decoder reconstructs the original data from the encoded parameters whilst minimizing the losses. The layer with the smallest number of neurons is called the latent space. From the latent space the encoded, or latent, representation of the input signal can be extracted.

The choice of dimensionality of the latent space is “problematic” [46]. In order to achieve maximum data compression, the number of neurons in the latent space of the autoencoder network should be as small as possible. However one would also like to be able to reconstruct the data with minimal error. If the inherent dimensionality of the data is not known *a priori* (as is typical) [46, 48, 49] but important, sparse autoencoder networks with Bayesian regularization methods should be used [50]. Furthermore, inference from the latent space representation is nontrivial because how the network “learns” to encode a signal in training is not necessarily unique.

In this work, we examine how an autoencoder network consisting solely of dense layers can be employed for direct extraction of the parameters of a signal with well-defined functional form from the latent signal-representation of an autoencoder network, as this becomes relevant in real-time signal analysis. To achieve such a task, we must make sure that (1) the dimensionality of the latent space matches the dimensionality of the input signal, and (2) that the autoencoder network encodes the input signal in a specific way where the latent representation of the signal matches the independent parameters of the signal.

We are able to satisfy the first requirement because the number of parameters in our signal’s functional form are known, which allows us to match the number of neurons in the latent space of the autoencoder network to the number of parameters of the function (Secs. II B &

III B). Thereby we achieve efficient encoding without redundant neurons in the latent space, or redundant values in the latent representation of the signal. We are able to satisfy the second requirement by training the autoencoder network in a specific, three stage training method (Sec. III D).

## B. Model signals

We use autoencoder networks to estimate the parameters of two types of experimentally relevant model signals: (i) exponentially decaying signals and (ii) decaying oscillations.

### 1. Exponentially decaying signals

The first model signals that we investigate are exponentially decaying signals, as observed in many cavity ring down spectroscopy and cavity-enhanced spectroscopy and sensing methods (see Refs. [22–24] and references therein), and time-resolved fluorescence spectroscopy [51, 52]. An exponentially decaying signal can be characterized in terms of a model function as:

$$y(t) = A_0 \cdot e^{-t/\tau} + y_0, \quad (2)$$

where  $A_0$  is the initial amplitude and  $\tau$  is the decay constant of the signal,  $y_0$  is the signal offset and  $t$  is the independent (time) variable. Here, for simplicity and without loss of generality, we assume that  $A_0 = 1$  and restrict the investigation of noise contributions to the global offset parameter, i.e.  $y_0(t)$ . This way, the dimensionality of the decay function is reduced to a single parameter which for most cases of interest carries the valuable information; the decay constant  $\tau$ .

### 2. Decaying oscillations

The second type of model signals we investigate are decaying oscillations, as these become relevant in a wide range of experimental techniques, particularly within nuclear magnetic resonance (NMR) [13], optical magnetometry [15–19] and cavity-enhanced polarimetry [25–32] and ellipsometry [33–36]. We describe damped oscillating signals as:

$$y(t) = A_0 \cdot e^{-t/\tau} \cdot \cos(2\pi \cdot f \cdot t + \phi) + y_0, \quad (3)$$

where  $t$  is the independent variable of the signal (time),  $A_0$  is the oscillation's initial amplitude,  $\tau$  is the decay constant of the signals envelope,  $f$  is the frequency, and  $\phi$  is the phase of the oscillation. Finally  $y_0$  is the global signal offset. Again, we assume the amplitude to be normalized ( $A_0 = 1$ ) and no signal offset ( $y_0 = 0$ ) to simplify the neural network inputs. The experimentally relevant parameters  $\tau$ ,  $f$  and  $\phi$ , are the free parameters we extract from the latent representation. We recognize that, similar to the case of pure exponential decays, the amplitude parameter  $A_0$  could potentially be an experimentally relevant parameter for inspection purposes, and could be added to the free parameters in the model signal.

### 3. Signal-to-noise ratio

In the model signals, we define noise as contributions to the global offset parameter ( $y_0$ ), which we model to be normally distributed, i.e.,  $\langle y_0(t) \rangle = 0$ ,  $\langle y_0^2(t) \rangle = \sigma_{y_0}^2$ . As such we can define the signal-to-noise ratio as:  $\text{SNR} = A_0 / \sigma_{y_0}^2 = \sigma_{y_0}^{-2}$ . Under realistic experimental conditions, signal-amplitude fluctuations can be incorporated into the SNR through  $A_0$ .

### 4. Cramér-Rao lower bound

The Cramér-Rao lower bound (CRLB) defines a fundamental limit on the statistical uncertainty of an unbiased estimator of a parameter. For a given, damped signal (Eq. 2) & Eq. 3) the CRLB [16, 53] sets the lower limit on the variance of both the decay constant estimator  $\sigma_\tau^2$ , and the frequency estimator  $\sigma_f^2$ . In general, the CRLB limit can be defined for any parameter extracted by an unbiased estimator. Here however, we focus on the two most important parameters for the experimental techniques of interest, e.g. [13–36, 51, 52].

The relation between the variance limit of the data-time estimator and the lower limit of the frequency estimator is given by:  $\sigma_\tau^2 = 2\pi \sigma_f^2$ . The CRLB for the frequency estimator  $\sigma_f^2$  is given by [16, 53]:

$$\sigma_f^2 = \frac{6}{(2\pi)^2 \text{SNR}^2 f_{\text{BW}} T_m^3} \xi(\tau/T_m), \quad (4)$$

where SNR is the signal-to-noise ratio of the signal;  $f_{\text{BW}}$  is the sampling-rate-limited bandwidth of the measurement;  $T_m$  is the measurement time window;  $\xi(\tau/T_m)$  is a correction factor that takes into account the signal decay, which is given by [16, 53]:

$$\xi(r) = \frac{\exp(2/r) - 1}{3r^3 \cosh(2/r) - 3r(r^2 + 2)}. \quad (5)$$

The factor  $\xi(\tau/T_m)$  serves as a compensation factor in Eq. 4 that penalizes measurement of the tails of the exponential decay when the signal has effectively died out. The validity of Eq. 4 hinges on the assumption that the period of the oscillation is shorter than the typical decay time ( $\tau$ ) of the signal envelope, and that a sufficient number of oscillations occur in the measurement time window. However, in the absence of oscillations, the relationship between  $\sigma_f^2$  and  $\sigma_\tau^2$  is still valid. Moreover, Eq. 4 dictates that any noise sources affecting the signal detection are contributing to the fundamental CRLB limit through their effect on the SNR of signal.

In Ref. [31], it was demonstrated that the CRLB limit is the appropriate estimator of the fundamental sensitivity of frequency-based measurements within the context of cavity-enhanced spectro-polarimetric techniques.

## III. Methods

### A. Simulated signals and data-sets

We use simulated signals following model equations (Eqs. 2 & 3) to demonstrate the parameter-extraction capabilities of dense autoencoder networks. We simulate signals with a duration of  $5\ \mu\text{s}$  with an effective

bandwidth-limited sampling rate of 200 MHz, resulting in discretely sampled signals with a length of 1000 samples. These conditions are comparable to signals from an experimental continuous-wave cavity ring-down polarimetry setup [31]. We vary the experimentally relevant parameters in the decaying signals that we use to train the autoencoder networks. For exponentially decaying signals (Eq. 2), the only parameter of interest is the decay constant  $\tau$ , which we vary between signals as follows:

$$\tau = |\text{norm}(\mu_\tau = 1 \mu\text{s}, \zeta_\tau = 0.5 \mu\text{s})|, \quad (6)$$

where  $\mu_\tau$  and  $\zeta_\tau$  are the average and standard deviation of a normal distribution, from which we take the absolute value. Therefore, a typical simulated signal has a decay constant  $\tau = 1 \mu\text{s}$  and a measurement time window  $T_m = 5\tau = 5 \mu\text{s}$ . For the decaying oscillations (Eq. 3) we vary the decay constant using the same process, but also vary the other two parameters of interest, the frequency and phase of the oscillation,  $f$  and  $\phi$  respectively, using:

$$f = \text{norm}(\mu_f = 3 \text{ MHz}, \zeta_f = 0.1 \text{ MHz}) \quad (7)$$

$$\phi = \text{norm}(\mu_\phi = 0, \zeta_\phi = 0.1) \quad (8)$$

For the exponentially decaying signals a training data set consists of 200 signals, while for the decaying oscillations, a training data set consists of 1000 signals. These signals have a SNR = 2<sup>20</sup>, to allow the autoencoder network to learn the features of each model signal and the signals variance under changing underlying parameters of interest.

### B. Dense autoencoder networks

The autoencoder networks that we use to reconstruct, and extract the parameters from decaying signals, have an input layer and output layer of 1000 neurons, equal to the number of samples in a signal. However the number of neurons in the latent space of the autoencoder networks are different between autoencoder networks that analyze exponentially decaying signals and decaying oscillations. In the case of the exponentially decaying signals, we use a network with only a single neuron in the latent space, corresponding with the single parameter of interest that we wish to extract from the signal. In the case of the decaying oscillations, we need three neurons in the latent space of the network in order to be able to extract the three interesting parameters of that signal. Furthermore, the signal complexity of a decaying oscillation with three parameters is higher than a exponentially decaying signal with only one parameter of interest, therefore not only is the size of the latent space different between these networks, but also also the number of neurons in the layers of the encoder and decoder part of the autoencoder network (Fig. 2) has to be different for the networks that analyse the two different model signals. The network we use to analyse the exponentially decaying signal has a shape of 1000-50-1-50-1000 neurons per layer respectively. For the decaying oscillations, we use

a network with a shape of 1000-50-10-3-10-50-1000 neurons per layer. The sizes of the networks were determined by evaluating the performance of various sizes of networks and choosing the smallest network with precise and accurate results. We choose to use a hyperbolic tangent as activation function for all relevant layers. This choice allows the neural network to express values between -1 and 1, which matches the range of the input and output signals. We create the aforementioned neural networks using the Tensorflow and Tensorflow.keras libraries in a homemade Python script.

### C. Signal reconstruction and parameter extraction

Typically, autoencoder networks are used to reconstruct the original input data. However, we wish to also extract the signal parameters directly from the latent space representation of the data. To do this we map the parameters of interest to a number between -1 and 1 that the autoencoder network can express in the latent space:

$$x_{\text{lat}} = \frac{x - \mu_x}{3 \times \zeta_x}, \quad (9)$$

where  $x_{\text{lat}}$  is the latent representation of the value of parameter  $x$  ( $\tau$ ,  $f$ , and  $\phi$ ).  $\mu_x$  and  $\zeta_x$  are the mean and standard deviation of the parameter variation defined in Eqs. 6-8. We use Eq. 9 to create a desired latent representation of signal's parameters during training, and to decode the latent representation back into the signal's parameter when using the autoencoder network to analyse signals. For a trained neural network, a signal only needs to be passed through the encoding part of the network, up to the latent space, in order to find the latent representation of the signal. To investigate the analysis speed of the neural networks, we only take into account the time it takes to encode the original signal into the latent representation.

### D. Training protocol

The autoencoder networks are trained using a stochastic gradient decent (SGD) algorithm and following a three-stage training scheme. Even though the sizes of the autoencoder networks are different given the two different model signals, the training method for the autoencoder networks is the same:

1. The complete autoencoder network is trained to recreate the input signals for 100 epochs
2. The encoder part of the autoencoder network, up to the latent space, (Fig. 2) is trained with input signals, and the desired latent-signal representation as output for 100 epochs.
3. Finally, the decoder part of the autoencoder network is trained with the desired latent-signal representation as input and the desired signals as output for 100 epochs.

We repeat these steps 10 times after which a new training data set is generated to avoid over-fitting a single data set. In total, each network is trained on 10 different data sets. By distinguishing three distinct training steps we are able to train the neural network to not only function as an autoencoder, recreating the original signal, but also allows us teach the autoencoder network to encode the signal in a specific way, that allows extraction of the signal parameters directly from the latent space of the autoencoder, satisfying the second requirement mentioned in Sec II A.

Figure 3 compares the average loss per neuron of two identical networks during training. The first network (coloured dots) is trained using our three-stage training method while the second network (grey line) is only trained on replicating the input data (step 1). Both networks encode and reconstruct exponentially decaying signals. It can clearly be seen that both training methods converge to similar losses per neuron at the end of training for the complete autoencoder networks (black dots vs. grey line). However, in the autoencoder network that is trained using our three-stage training method, we also see a decrease in losses from the encoder part of the autoencoder network (red dots), indicating that by using the three-stage training method we can achieve a desired latent signal representation without loss of the capabilities of the autoencoder network to reconstruct the original signal.

## IV. Results

### A. Exponentially decaying signals

Figure 4 shows the results for a trained autoencoder network reconstructing and extracting parameters from a exponentially decaying signals. The ability of the autoencoder network to extract the signal parameters from the latent space is compared to the performance of an ordinary least squares algorithm [31]. In Fig. 4(a) we show an example of a randomly generated, exponentially decaying signal with a time constant  $\tau = 1.81 \mu\text{s}$  and  $\text{SNR} = 2^5$ . We use a trained autoencoder network (Sec. III D) to reconstruct the signal and fit the signal to Eq. 2 using a least squares algorithm. The decay constant found by the least squares method is  $\tau = 1.81(2) \mu\text{s}$ . In Fig. 4(b) we show a histogram of 500 estimates of the decay constant extracted from the latent space of the autoencoder network. By subtracting the least squares decay constant estimate ( $\tau_{\text{est}}$ ) and fitting the histogram to a Gaussian distribution we show that there is no difference in accuracy between the two analysis methods as the center of the distribution is not significant from zero. The width of the distribution of the decay constant estimates coincides with the uncertainty of the least squares estimation method indicating that also the precision of the two methods is equal. In Fig. 4(c) we demonstrate that the parameter extraction methodology we employ here based on autoencoder networks, is also able to, accurately and without loss in precision, follow signal changes. In particular, we examine a scenario where the time constants

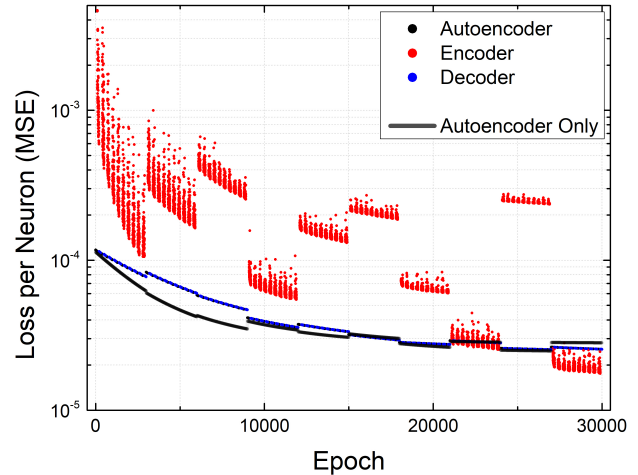


FIG. 3. Average mean squared error (MSE) loss per neuron as a function of training epochs for the three-stage training method (coloured dots) compared to typical training of an autoencoder network (grey line). The black, red and blue dots correspond to the losses at training step 1, 2 and 3 respectively (see text). The networks have the same shape and size, are trained for an equal number of epochs using an equal amount of training data. The data points of the complete autoencoder training (black dots) overlap with the decoder training data points (blue dots). The breaks in the losses of the encoder network training (red dots) when a new dataset is generated are attributed to the small number of neurons in the latent space of the autoencoder network and the specifics of the small validation data set.

of different input decaying signals change by 30% following a characteristic dispersive (Lorentzian) profile, which simulates a possible experimental scenario where spectroscopy of absorptive features in real-time is required as in the case of, for instance, trace-gas detection using cavity ring-down spectroscopy [54, 55]. Figure 4(d) demonstrates that the precision of the neural network is able to match the precision of the least squares algorithm and, thus, both are limited by the CRLB over several orders of magnitude in signal-to-noise ratio even though the SNR is not varied within the training data sets during the training of the autoencoder network.

### B. Decaying oscillations

In Fig. 5 we present the results of a trained autoencoder network reconstructing and extracting parameters from decaying oscillations. In Fig. 5(a) we show an example of a decaying oscillating signal with  $\text{SNR} = 2^5$ ,  $\tau = 1.28 \mu\text{s}$ ,  $\phi = -0.243$ , and  $f = 2.972 \text{ MHz}$ . We fit the signal to Eq. 3 using a least squares algorithm and use a trained autoencoder (Sec. III D) to reconstruct the signal. Figure 5(b) shows the histograms of 500 parameter estimates of  $\tau$ ,  $\phi$  and  $f$ , extracted from the latent space of the autoencoder network. We extract the latent parameters  $\tau_{\text{lat}}$ ,  $\phi_{\text{lat}}$ ,  $f_{\text{lat}}$  from the latent space of the autoencoder network and use Eq. 9 to reconstruct the estimate of the signal pa-

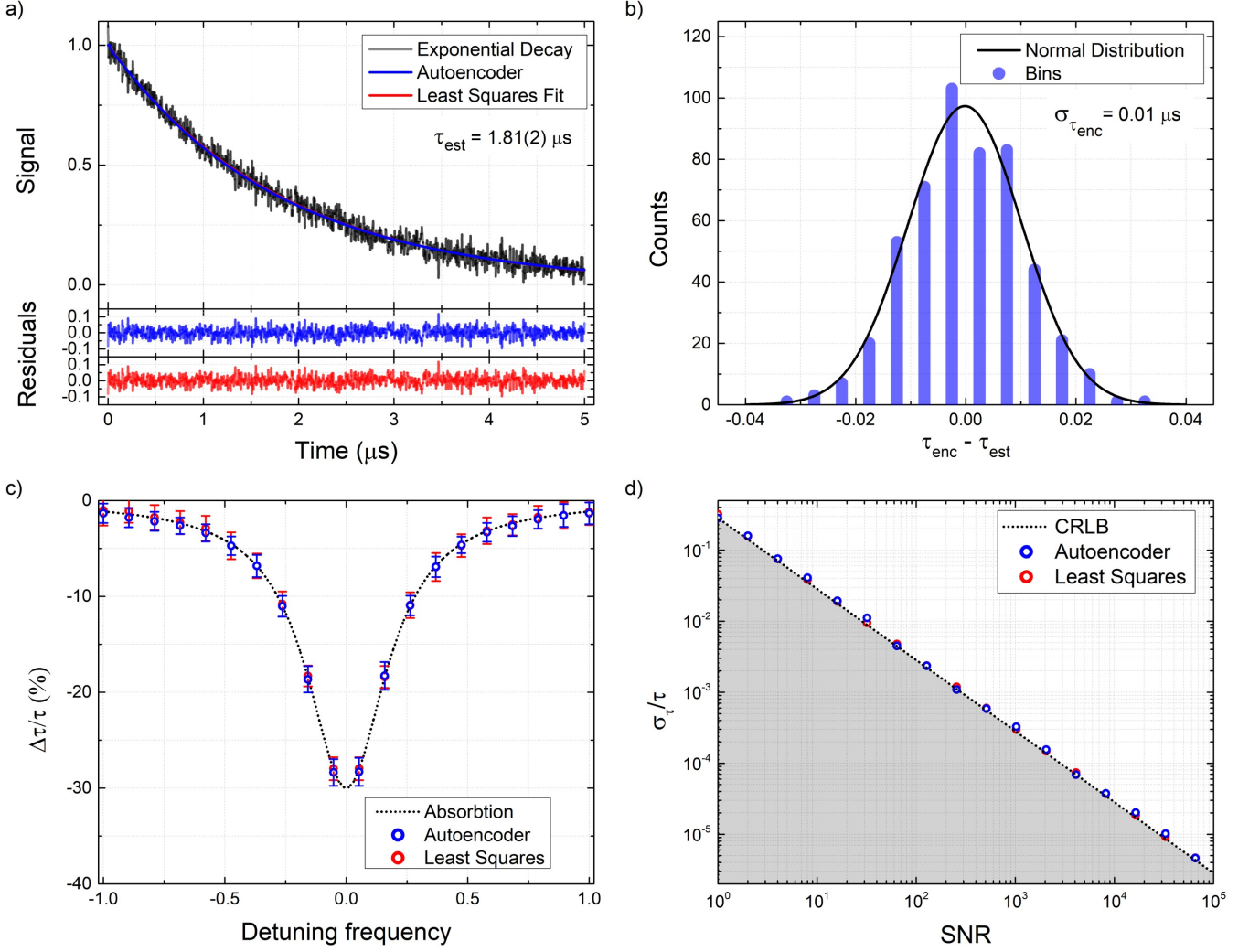


FIG. 4. Exponentially decaying signal parameter extraction using an autoencoder network. (a) Example of an exponentially decaying signal with 1000 samples and  $\text{SNR} = 2^5$  (black line) reconstructed by a trained autoencoder network (blue line) and analyzed using a least squares fitting method (red line). The residuals for each method are shown at the bottom. The decay constant estimated by the least squares method is  $\tau_{\text{est}} = 1.81(2) \mu\text{s}$ . (b) Histogram of 500 decay-constant estimates extracted from the latent space of the trained autoencoder network. Analysed signals have decay constants and SNR equal to the signal shown in (a). The value of the decay constant estimated by the least squares method,  $\tau_{\text{est}}$ , is subtracted from the decay constant extracted from the latent space of the autoencoder network,  $\tau_{\text{enc}}$ . The full width at half maximum (FWHM) width of the fitted Gaussian distribution coincides with the uncertainty of the least squares method while the center of the distribution is not significantly different from 0. (c) Accurate and precise signal parameter extraction using an autoencoder network is possible in the case of (relative) changes in the decay constant through a simulated absorption feature (dotted line) as one would expect in, for instance, cavity ring-down absorption spectroscopy when a laser is detuned from the resonance frequency of the absorption feature. The feature is followed by both the trained autoencoder network (blue dots) and a least squares algorithm (red dots). The error bars represent the standard deviation of 100 parameter estimations from the latent space of the trained autoencoder network and the least squares algorithm respectively. (d) Precision of a least squares algorithm and a trained autoencoder network on estimating the decay constant from the latent space over multiple orders of magnitude in SNR. The Cramér-Rao lower bound (CRLB) giving the fundamental estimation limit on the decay constant is also shown (dotted line) and the area below the fundamental estimation limit is greyed out.

rameters found by the autoencoder  $\tau_{\text{enc}}, \phi_{\text{enc}}, f_{\text{enc}}$ . From each parameter  $x_{\text{enc}}$  we subtract the parameter's estimated value obtained through the least squares method  $x_{\text{est}}$  (where  $x$  substitutes  $\tau$ ,  $\phi$  and  $f$  respectively) and fit the histograms to a Gaussian distribution. Each dis-

tribution has a center that is not significant from zero and a width equal to the uncertainty of the fit parameters found by the least squares fit indicating that there is no difference in accuracy or precision between the two analysis methods. In Fig. 5(c) we demonstrate that the

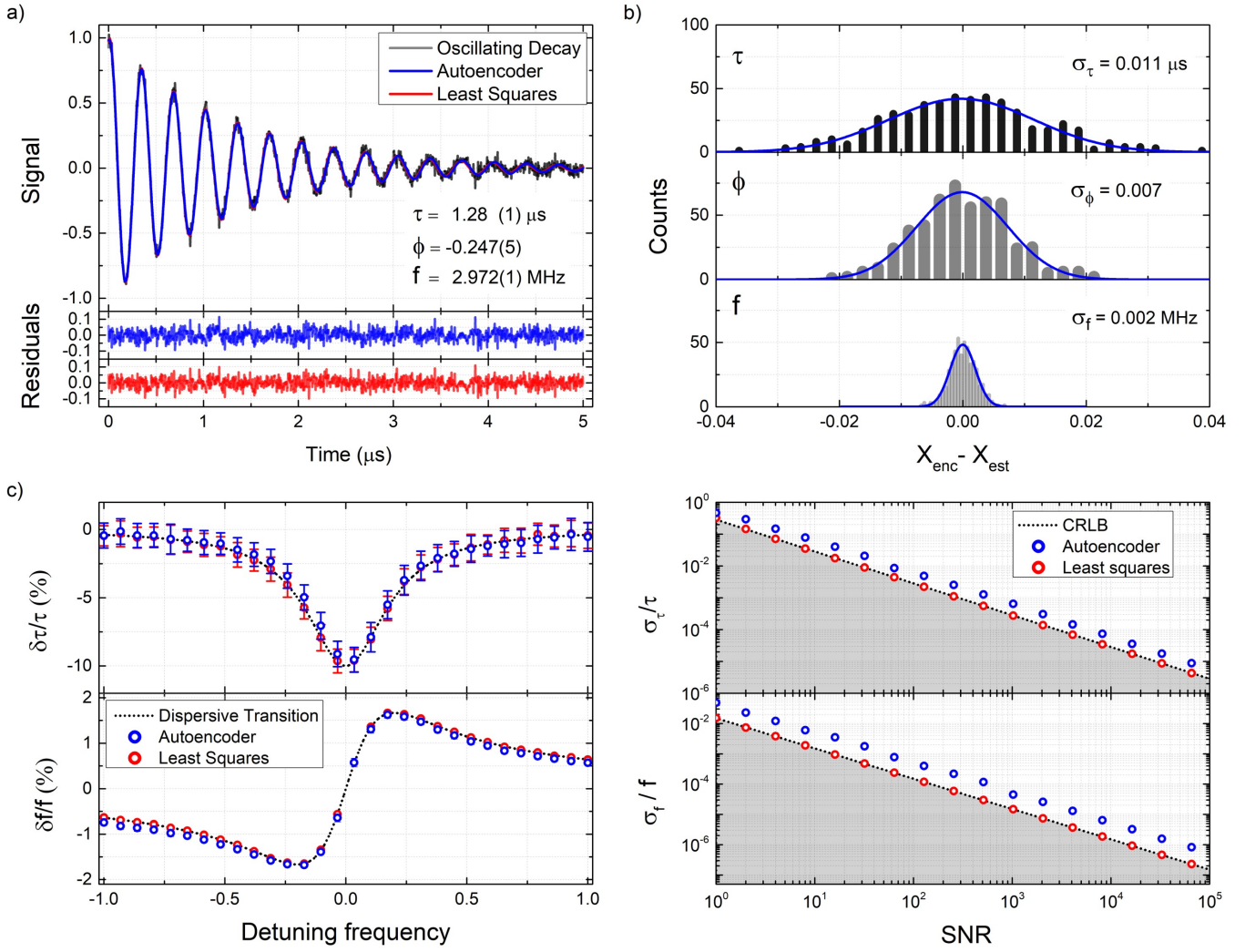


FIG. 5. Parameter estimation of the autoencoder network compared to a least squares algorithm for exponentially decaying oscillations. (a) Example of a decaying oscillation (black line) with  $\text{SNR} = 2^5$  reconstructed by a trained autoencoder network (blue line) and a least squares fit (red line). The residuals for each method are shown in the bottom insets with their corresponding colour. The signal parameters found by the least squares fit are shown in the figure with their uncertainties. (b) Histograms of 500 signal parameter sets (top:  $\tau$ , middle:  $\phi$  and bottom:  $f$ ) extracted from the latent space of the autoencoder network. The analysed signals have the same parameters and SNR as the example signal shown in (a). For each of the signals parameters, we subtract the parameter estimate of the least squares fit  $X_{est}$  from the parameter estimate extracted latent space of the autoencoder network  $X_{enc}$ . The width of the fitted Gaussian distributions coincide with the uncertainty of the least squares method for each individual parameter of the signal and the centers of the distributions are not significantly different from 0. (c) Accurate and precise signal parameter extraction using an autoencoder network is possible in the case of (relative) changes in the decay constant through a simulated dispersive absorption feature, or cotton effect, (dotted line) as one would expect in a cavity enhanced polarimetry experiment when a laser is detuned from the resonance frequency of the absorption feature. The feature is followed by both the trained autoencoder network (blue dots) and the least squares algorithm (red dots). The error bars represent the standard deviation of 100 parameter estimations from the latent space of the trained autoencoder network and the least squares algorithm respectively. (d) Precision of the trained autoencoder network (blue dots) and the least squares algorithm (red dots) in estimating both the frequency ( $f$ ) and decay constant ( $\tau$ ) over several orders of magnitude in SNR. The fundamental estimation limits of these parameters, given by the Cramér-Rao lower bound (CRLB) is also shown (dotted line) and the area below the fundamental estimation limit is greyed out.

trained autoencoder network is able to, accurately and without loss in precision, follow signal changes. More specifically, we investigate a simulated absorption feature where both the frequency and decay constant of the in-

put signal are changing following a dispersive line profile (cotton effect). Finally, in Fig. 5(d) we show that the precision of the parameter estimates from the latent space of the trained autoencoder network on the estimation of the

frequency and decay constant follows the precision of the least squares method for five orders of magnitude in SNR. Moreover, the precision of the parameters extracted from the latent space of the autoencoder network is very close to the fundamental estimation limit given by the CRLB.

### C. Complexity vs. calculation time

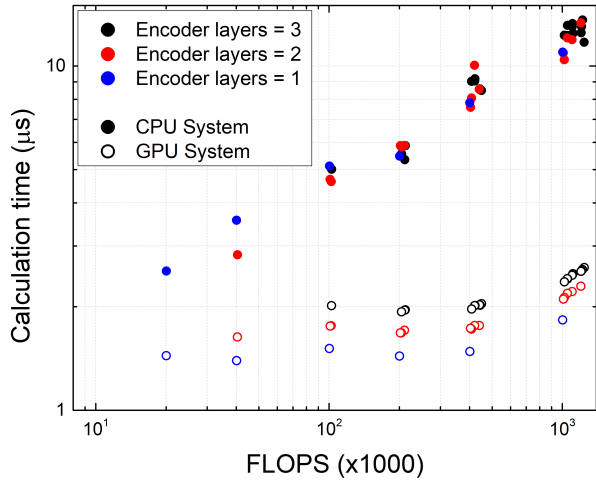


FIG. 6. Calculation time required by the encoder part of the autoencoder network to extract the latent parameters of a single damped oscillating signal as a function of floating point operations (FLOPS) required to calculate the network using a CPU- (solid dots) and a GPU- (open dots) based system. The networks are varied in size, and thereby the required number of FLOPS needed to calculate latent signal representation. We vary the size of the network by varying the number of layers in the encoder network and the number of neurons within each layer. The lengths of these layers range from 10 to 500 neurons, where the smallest network investigated has a single layer with 10 neurons, and the largest network has 3 layers with 500, 200 and 100 neurons between the input layer and the latent space respectively.

Analysis speed is crucial for the real-time investigation and control of fast processes. Faster methods of analysis allow for large data stream to be analysed quicker, driving down computational costs. In previous work [43], it was shown that non-iterative FFT methods have a  $200\ \mu\text{s}$  calculation time and that a least squares fitting algorithm requires  $> 1\ \text{ms}$  of calculation time to analyse decaying oscillations of the same length that we consider in this paper using similar computational facilities to the systems used in this present work. Others have shown FPGA- based FFT algorithms for determining the decay constant of decaying signals with analysis rates of  $4.4\ \text{kHz}$  [40]. Here, we show that trained autoencoder networks are able to analyse incoming signals significantly faster than previously reported methods. In particular, we compare the calculation speed of the encoder part of trained autoencoder networks of different sizes on different systems. We use a central processing unit (CPU-) and a graphics-processing unit (GPU-) based system to

investigate which system is most optimal for real-world implementation. The CPU-based system is based around an Intel(R) Xeon(R) W-2123, 3.6 GHz processing unit with access to 16 GB of random-access memory (RAM) with a frequency of 1330 MHz, while the GPU system is based on a NVIDIA Quadro p5000 graphics board. Both systems are cost-efficient and could reasonably be a part of a portable instrument.

In Fig. 6 we present the calculation time required by the encoder part of an autoencoder network to analyse a single decaying oscillation signal for varying sizes of networks. For the CPU calculation time we count the matrix multiplications, the adding/subtracting of the network biases and the application of the activation function towards the calculation time shown in Fig. 6. Other pre-processing operations for the CPU-based system, such as data collection, take between  $3.6 - 4.9\ \mu\text{s}$  per signal and are not included. For the calculation time of the GPU system we include all processes happening using the GPU device, this includes not only the aforementioned operations such as matrix multiplications, the adding/subtracting of the network biases and the application of the activation function, but also the transfer time of the results of the encoder onto the RAM of the computer. We do not include the time it takes for the original signal to be transferred from the RAM onto the GPU memory ( $\sim 5\ \mu\text{s}$ ) or any other pre/post-processing operations conducted by the CPU of the system ( $\sim 6\ \mu\text{s}$ ). For the GPU-based system there is a clear difference in calculation time between neural networks with different numbers of layers in the encoder network, something we do not observe for the same neural networks on the CPU-based system. The results we show in Figs. 4 & 5 are obtained with autoencoder networks that require the calculation of  $\sim 100,000$  floating point operations (FLOPS) to reach the latent space representation of the signal. Using the trained autoencoder networks we are able to achieve analysis rates upwards of  $75\ \text{kHz}$  using the GPU-based system. This includes the data transfer time, the pre/post processing operations conducted by the CPU and the actual calculation time required of the autoencoder network itself. With optimization of the transfer rate between the data-acquisition system and data-analysis system and minimization of prepossessing operations, down to a combined  $\sim 3\ \mu\text{s}$ , the method of analysis we propose in this paper has the capabilities to achieve  $> 200\ \text{kHz}$  analysis rates given the  $< 2\ \mu\text{s}$  calculation time that we demonstrate with an accuracy closely following the fundamental estimation characteristics of the signal.

### V. Outlook and conclusion

In summary we have shown that we can extract parameters from decaying signals with an accuracy fundamentally limited by the signal characteristics using simple autoencoder networks. Moreover, we demonstrate that this method is orders of magnitude faster than a conventional least squares fitting method, regardless of CPU- or GPU implementation of the neural network. We demon-

strate analysis rates of 75 kHz for signals with 1000 samples and illustrate that higher analysis rates are achievable with optimization of data transfer speed between a data-acquisition and data-analysis device, which would allow for real time signal analysis rates of >200 kHz using state-of-the-art GSa/s sampling rates. These analysis rates open up new experimental methods where real-time data-analysis is crucial for experimental control.

Concluding, we wish to note that the methodology of signal parameter extraction directly from the latent space of dense autoencoder networks could be applicable to other signal types that currently use fitting models for parameter extraction. For instance: neural networks are currently used for the classification of spectroscopic data

[9–11], but we see no reason why the method we demonstrate in this paper could not directly analyse these kinds of spectroscopic signals to give quantitative results. Signals of higher complexity, such as signals with additional frequency components, or additional parameters in general, will require larger networks and larger training data sets for the network but we can see no fundamental limitations that would limit the widespread use of these types of analysing autoencoder networks.

### Acknowledgments

This work was supported by the European Commission Horizon 2020, project ULTRACHIRAL (Grant No. FETOPEN-737071).

---

[1] Bishop CM, et al. (1995) Neural networks for pattern recognition. Oxford university press

[2] Hertz JA (2018) Introduction to the theory of neural computation. CRC Press

[3] Gao C, Saraf A, Huang JB, Kopf J (2020) Flow-edge guided video completion. In: European Conference on Computer Vision, Springer, pp 713–729, <https://arxiv.org/abs/2009.01835>

[4] Shamir A, Mitra NJ, Umetani N, Koyama Y (2020) Intelligent tools for creative graphics. In: ACM SIGGRAPH 2020 Courses, pp 1–11, <https://doi.org/10.1145/3388769.3407498>

[5] Brown TB, Mann B, Ryder N, Subbiah M, Kaplan J, Dhariwal P, Neelakantan A, Shyam P, Sastry G, Askell A, et al. (2020) Language models are few-shot learners. arXiv preprint arXiv:200514165 <https://arxiv.org/abs/2005.14165>

[6] Carleo G, Cirac I, Cranmer K, Daudet L, Schuld M, Tishby N, Vogt-Maranto L, Zdeborová L (2019) Machine learning and the physical sciences. *Reviews of Modern Physics* 91(4):045002, <https://doi.org/10.1103/RevModPhys.91.045002>

[7] Sanchez-Gonzalez A, Godwin J, Pfaff T, Ying R, Leskovec J, Battaglia P (2020) Learning to simulate complex physics with graph networks. In: International Conference on Machine Learning, PMLR, pp 8459–8468, <http://proceedings.mlr.press/v119/sanchez-gonzalez20a.html>

[8] Peurifoy J, Shen Y, Jing L, Yang Y, Cano-Renteria F, DeLacy BG, Joannopoulos JD, Tegmark M, Soljačić M (2018) Nanophotonic particle simulation and inverse design using artificial neural networks. *Science advances* 4(6):eaar4206, <https://doi.org/10.1126/sciadv.aar4206>

[9] Wang J, Liao X, Zheng P, Xue S, Peng R (2018) Classification of chinese herbal medicine by laser-induced breakdown spectroscopy with principal component analysis and artificial neural network. *Analytical letters* 51(4):575–586, <https://doi.org/10.1080/00032719.2017.1340949>

[10] Del Moral F, Guillén A, Del Moral L, O’valle F, Martínez L, Del Moral R (2009) Duroc and iberian pork neural network classification by visible and near infrared reflectance spectroscopy. *Journal of Food Engineering* 90(4):540–547, <https://doi.org/10.1016/j.jfoodeng.2008.07.027>

[11] Gniadecka M, Philipsen PA, Wessel S, Gniadecki R, Wulf HC, Sigurdsson S, Nielsen OF, Christensen DH, Hercogova J, Rossen K, et al. (2004) Melanoma diagnosis by raman spectroscopy and neural networks: structure alterations in proteins and lipids in intact cancer tissue. *Journal of investigative dermatology* 122(2):443–449, <https://doi.org/10.1046/j.0022-202X.2004.22208.x>

[12] Nottbeck N, Schmitt C, Büscher V (2019) Implementation of high-performance, sub-microsecond deep neural networks on FPGAs for trigger applications. *Journal of Instrumentation* 14(09):P09014, <https://doi.org/10.1088/1748-0221/14/09/P09014>

[13] Günther H (2013) NMR spectroscopy: basic principles, concepts and applications in chemistry. John Wiley & Sons

[14] Budker D, Romalis M (2007) Optical magnetometry. *Nature physics* 3(4):227–234, <https://doi.org/10.1038/nphys566>

[15] Savukov I, Romalis M (2005) NMR detection with an atomic magnetometer. *Physical review letters* 94(12):123001, <https://doi.org/10.1103/PhysRevLett.94.123001>

[16] Gemmel C, Heil W, Karpuk S, Lenz K, Ludwig C, Sobolev Y, Tullney K, Burghoff M, Kilian W, Knappe-Grüneberg S, et al. (2010) Ultra-sensitive magnetometry based on free precession of nuclear spins. *The European Physical Journal D* 57(3):303–320, <https://doi.org/10.1140/epjd/e2010-00044-5>

[17] Nikiel A, Blümller P, Heil W, Hehn M, Karpuk S, Maul A, Otten E, Schreiber LM, Terekhov M (2014) Ultrasensitive <sup>3</sup>He magnetometer for measurements of high magnetic fields. *The European Physical Journal D* 68(11):1–12, <https://doi.org/10.1140/epjd/e2014-50401-3>

[18] Grujić ZD, Koss PA, Bison G, Weis A (2015) A sensitive and accurate atomic magnetometer based on free spin precession. *The European Physical Journal D* 69(5):135, <https://doi.org/10.1140/epjd/e2015-50875-3>

[19] Hunter D, Piccolomo S, Pritchard J, Brockie N, Dyer T, Riis E (2018) Free-induction-decay magnetometer based on a microfabricated cs vapor cell. *Physical Review Applied* 10(1):014002, <https://doi.org/10.1103/PhysRevApplied.10.014002>

[20] Wheeler MD, Newman SM, Orr-Ewing AJ, Ashfold MN (1998) Cavity ring-down spectroscopy. *Journal of the Chemical Society, Faraday Transactions* 94(3):337–351, <https://doi.org/10.1039/A707686J>

[21] Romanini D, Kachanov A, Sadeghi N, Stoeckel F (1997) CW cavity ring down spectroscopy. *Chemical Physics Letters* 264(3-4):316–322, [https://doi.org/10.1016/S0009-2614\(96\)01351-6](https://doi.org/10.1016/S0009-2614(96)01351-6)

[22] Berden G, Peeters R, Meijer G (2000) Cavity ring-down spectroscopy: Experimental schemes and applications. *International reviews in physical chemistry* 19(4):565–607

[23] Berden G, Engeln R (2009) Cavity ring-down spectroscopy: techniques and applications. John Wiley & Sons, <https://doi.org/10.1080/014423500750040627>

[24] Gagliardi G, Loock HP (2014) Cavity-enhanced spectroscopy and sensing, vol 179. Springer, <https://doi.org/10.1007/978-3-642-40003-2>

[25] Müller T, Wiberg KB, Vaccaro PH (2000) Cavity ring-down polarimetry (CRDP): a new scheme for probing circular birefringence and circular dichroism in the gas phase. *The Journal of Physical Chemistry A* 104(25):5959–5968, <https://doi.org/10.1021/jp000705n>

[26] Müller T, Wiberg KB, Vaccaro PH, Cheeseman JR, Frisch MJ (2002) Cavity ring-down polarimetry (CRDP): theoretical and experimental characterization. *JOSA B* 19(1):125–141, <https://doi.org/10.1364/JOSAB.19.000125>

[27] Sofikitis D, Bougas L, Katsoprinakis GE, Spiliotis AK, Loppinet B, Rakitzis TP (2014) Evanescent-wave and ambient chiral sensing by signal-reversing cavity ring-down polarimetry. *Nature* 514(7520):76–79, <https://doi.org/10.1038/nature13680>

[28] Bougas L, Sofikitis D, Katsoprinakis GE, Spiliotis AK, Tzallas P, Loppinet B, Rakitzis TP (2015) Chiral cavity ring down polarimetry: Chirality and magnetometry measurements using signal reversals. *The Journal of Chemical Physics* 143(10):09B603.1, <https://doi.org/10.1063/1.4930109>

[29] Dupré P (2015) Birefringence-induced frequency beating in high-finesse cavities by continuous-wave cavity ring-down spectroscopy. *Physical Review A* 92(5):053817, <https://doi.org/10.1103/PhysRevA.92.053817>

[30] Spiliotis A, Xygkis M, Klironomou E, Kardamaki E, Boulogiannis G, Katsoprinakis G, Sofikitis D, Rakitzis T (2020) Optical activity of lysozyme in solution at 532 nm via signal-reversing cavity ring-down polarimetry. *Chemical Physics Letters* p 137345, <https://doi.org/10.1016/j.cplett.2020.137345>

[31] Visschers JC, Tretiak O, Budker D, Bougas L (2020) Continuous-wave cavity ring-down polarimetry. *The Journal of Chemical Physics* 152(16):164202, <https://doi.org/10.1063/5.0004476>

[32] Bougas L, Katsoprinakis G, Von Klitzing W, Sapirstein J, Rakitzis T (2012) Cavity-enhanced parity-nonconserving optical rotation in metastable xe and hg. *Physical review letters* 108(21):210801, <https://doi.org/10.1103/PhysRevLett.108.210801>

[33] Papadakis V, Everest MA, Stamatakis K, Tzortzakis S, Loppinet B, Rakitzis TP (2011) Development of cavity ring-down ellipsometry with spectral and submicrosecond time resolution. In: *Instrumentation, Metrology, and Standards for Nanomanufacturing, Optics, and Semiconductors V*, International Society for Optics and Photonics, vol 8105, p 81050L

[34] Stamatakis K, Papadakis V, Everest MA, Tzortzakis S, Loppinet B, Rakitzis TP (2013) Monitoring adsorption and sedimentation using evanescent-wave cavity ring-down ellipsometry. *Applied Optics* 52(5):1086–1093

[35] Sofikitis D, Stamatakis K, Everest MA, Papadakis V, Stehle JL, Loppinet B, Rakitzis TP (2013) Sensitivity enhancement for evanescent-wave sensing using cavity-ring-down ellipsometry. *Optics Letters* 38(8):1224–1226, <https://doi.org/10.1364/OL.38.001224>

[36] Sofikitis D, Spiliotis A, Stamatakis K, Katsoprinakis G, Bougas L, Samartzis P, Loppinet B, Rakitzis T, Surligas M, Papadakis S (2015) Microsecond-resolved sdr-based cavity ring down ellipsometry. *Applied Optics* 54(18):5861–5865, <https://doi.org/10.1364/AO.54.005861>

[37] Halmer D, von Basum G, Hering P, Mürtz M (2004) Fast exponential fitting algorithm for real-time instrumental use. *Review of scientific instruments* 75(6):2187–2191, <https://doi.org/10.1063/1.1711189>

[38] Mazurenka M, Wada R, Shillings A, Butler T, Beames J, Orr-Ewing A (2005) Fast fourier transform analysis in cavity ring-down spectroscopy: application to an optical detector for atmospheric NO<sub>2</sub>. *Applied Physics B* 81(1):135–141, <https://doi.org/10.1007/s00340-005-1834-1>

[39] Everest MA, Atkinson DB (2008) Discrete sums for the rapid determination of exponential decay constants. *Review of Scientific Instruments* 79(2):023108, <https://doi.org/10.1063/1.2839918>

[40] Bostrom G, Atkinson D, Rice A (2015) The discrete fourier transform algorithm for determining decay constants—implementation using a field programmable gate array. *Review of Scientific Instruments* 86(4):043106, <https://doi.org/10.1063/1.4916709>

[41] Aboutanios E (2009) Estimation of the frequency and decay factor of a decaying exponential in noise. *IEEE Transactions on Signal Processing* 58(2):501–509, <https://doi.org/10.1109/TSP.2009.2031299>

[42] Aboutanios E (2011) Estimating the parameters of sinusoids and decaying sinusoids in noise. *IEEE Instrumentation & Measurement Magazine* 14(2):8–14, <https://doi.org/10.1109/MIM.2011.5735249>

[43] Visschers JC, Wilson E, Conneely T, Mudrov A, Bougas L (2021) Rapid parameter determination of discrete damped sinusoidal oscillations. *Opt Express* 29(5):6863–6878, <https://doi.org/10.1364/OE.411972>

[44] van Veen & S Leijnen F (2019) The neural network zoo. <https://www.asimovinstitute.org/neural-network-zoo/>

[45] Bourlard H, Kamp Y (1988) Auto-association by multi-layer perceptrons and singular value decomposition. *Biological cybernetics* 59(4-5):291–294, <https://doi.org/10.1007/BF00332918>

[46] DeMers D, Cottrell GW (1993) Non-linear dimensionality reduction. In: *Advances in neural information processing systems*, pp 580–587

[47] Hinton GE, Salakhutdinov RR (2006) Reducing the dimensionality of data with neural networks. *science* 313(5786):504–507, <https://doi.org/10.1126/science.1127647>

[48] Theis L, Shi W, Cunningham A, Huszár F (2017) Lossy image compression with compressive autoencoders.

arXiv preprint arXiv:1703.00395 <https://arxiv.org/abs/1703.00395>

[49] Lu X, Tsao Y, Matsuda S, Hori C (2013) Speech enhancement based on deep denoising autoencoder. In: Interspeech, vol 2013, pp 436–440

[50] Ng A, et al. (2011) Sparse autoencoder. CS294A Lecture notes 72(2011):1–19

[51] Boens N, Qin W, Basarić N, Hofkens J, Ameloot M, Pouget J, Lefevre JP, Valeur B, Gratton E, VandeVen M, et al. (2007) Fluorescence lifetime standards for time and frequency domain fluorescence spectroscopy. Analytical chemistry 79(5):2137–2149, <https://doi.org/10.1021/ac062160k>

[52] Cundall R (2013) Time-resolved fluorescence spectroscopy in biochemistry and biology, vol 69. Springer

Science & Business Media

[53] Yao YX, Pandit SM (1995) Cramér-Rao lower bounds for a damped sinusoidal process. IEEE Transactions on signal processing 43(4):878–885, <https://doi.org/10.1109/78.376840>

[54] Wahl EH, Tan SM, Koulakov S, Kharlamov B, Rella CR, Crosson ER, Biswell D, Paldus BA (2006) Ultra-sensitive ethylene post-harvest monitor based on cavity ring-down spectroscopy. Optics express 14(4):1673–1684, <https://doi.org/10.1364/OE.14.001673>

[55] Li Z, Hu R, Xie P, Chen H, Liu X, Liang S, Wang D, Wang F, Wang Y, Lin C, et al. (2019) Simultaneous measurement of NO and NO<sub>2</sub> by a dual-channel cavity ring-down spectroscopy technique. Atmospheric Measurement Techniques 12(6):3223–3236, <https://doi.org/10.5194/amt-12-3223-2019>